

Manufacturable blazed metasurface gratings designed by 3D topology optimization model

Simon Ans^{1,2}, Frédéric Zamkotsian¹, and Guillaume Demésy²

¹Aix Marseille Univ, CNRS, CNES, LAM, Marseille, France

²Aix Marseille Univ, CNRS, Centrale Med, Institut Fresnel, Marseille, France

Abstract

We present the generalization of our FEM-based topology optimization framework to 3D blazed metasurfaces operating in reflection over the visible and near-infrared range [400–1,500] nm. The design region is described through a density-based SIMP interpolation and optimized using the adjoint method, enabling the treatment of several tens of thousands degrees of freedom. A first approach directly applies topology optimization to the 3D Finite Element mesh (mesh-based), yielding a freeform structure that achieves an average diffraction efficiency of 62% in order -1 over two octaves under the targeted incidence. However, such patterns remain difficult to manufacture. We therefore introduce a pillar-based parameterization, embedding fabrication constraints within the optimization loop. The resulting binary metasurface, compatible with e-beam lithography and Reactive Ion Etching techniques, achieves an average efficiency of 57% over the same spectral band in s -polarization, with low polarization dependence. This work demonstrates that large-scale 3D topology optimization can bridge the gap between broadband optical performance and realistic nanofabrication constraints for blazed metasurfaces.

Keywords: Blazed gratings, Metasurface, Broadband optimization, Topology optimization, Maxwell's equations, Finite Element Method.

1 Introduction

Spectrographs are widely used in physics, biology and medicine, for material characterization purposes. Knowing the composition of a material with a non-invasive method is of paramount interest, allowing for the identification of molecules or atoms in living beings. This is the basis of disease diagnoses for instance, and broadly speaking of every kind of quality control for the environment and in the industry. For Earth and Universe Observation, spectroscopy allows us to identify atomic and molecular species, to measure redshifts in deep-field observations, to characterize exoplanetary atmospheres and to monitor ecosystems, mineral compositions, or pollution phenomena.

Blazed gratings are fundamental optical components in spectrographs, especially for studying low-flux radiation. The most common type, whose fabrication has been industrialized for certain applications, is the sawtooth-profiled grating (see Fig. 1, in reflection). It has a period above the considered wavelengths to deflect light on diffraction orders, while its so-called *blazed* geometry privileges a sole order for Signal-to-Noise (SNR) increase purpose. For visible (Vis) and Near Infrared (NIR) study, their pattern size is therefore around several micrometers. Although they demonstrate a high-level and robust blazing effect on one octave – from one wavelength to its double – the lack of possible

improvements in their design nudged the community toward developing subwavelength structures, commonly referred to as *metasurfaces* in the literature.

The first studies on blazed metasurfaces date back to the early 1990s and were published in Ref. [1]. The concept was later popularized by P. Lalanne et al. through the design and fabrication of a blazed metasurface operating in Vis and NIR, which they compared to a sawtooth blazed grating [2]. The promising results they obtained led the authors to discuss the natural improvements of their work. On the one hand, they suggested using computational electromagnetics to solve Maxwell's equations for a given structure. Two widely used numerical methods are the Rigorous Coupled Wave Analysis (RCWA) [3] and the Finite Element Method (FEM) [4], both allowing the resolution of Partial Differential Equations (PDEs) through spatial and temporal discretization. The second one is chosen in this article for its flexibility in design and implementation. On the other hand, the authors invited the reader to locally adjust the structure's geometry and improve its performance through mathematical and computational techniques.

The numerical resolution of PDEs with the FEM has been a major breakthrough in Computational Physics and Engineering. Physical problems involving realistic geometries could be solved numerically in many fields, such as fluid mechanics (Navier-Stokes equation), solid mechanics (convection-diffusion equations, dynamics equations), thermodynamics (heat equation), acoustics (wave equation) and of course photonics (Maxwell's equations). The idea of modifying the discretized domain to optimize its performance followed naturally. By "performance", we mean a given *objective function* to be improved (e.g., the resistance of a structure or efficiency of a device), which is also called target or merit function. The concept of structural optimization based on FEM appeared in the 1960s, introduced by L. Schmit's group according to Ref. [5]. Modifying the *design region* and its so-called *discretization mesh* constitutes shape optimization, which remains widely used today. The works of G. Allaire [6] are often cited as a reference in this domain.

The issues raised by shape optimization, such as mesh adaptation or sensitivity analysis – that have been addressed ever since [7, 8] – have caused another optimization method to emerge in the late 1980s: Topology Optimization (TO), introduced in Ref. [9]. Instead of modifying shape boundaries, TO finds the optimal design by directly changing the material distribution within small elementary "boxes", called voxels (a blend of "volume" and "pixel"). These voxels are defined once and for all at the start of the computation, allowing the Finite Element (FE) mesh to remain fixed. The numerous improvements of this method, mainly attributed to M. P. Bendsøe, O. Sigmund [10] and their collaborators, have established TO as a powerful and versatile design framework. At first developed for solid mechanics, it is now applied to any field governed by PDEs. A non-exhaustive list includes fluid mechanics and fluid-structure interactions [11, 12], acoustics [13, 14], electromechanics [15, 16] and photonics [17, 18, 19]. The latter is the domain of interest for this work.

More specifically, TO in nanophotonics has been largely developed thanks to the heuristic homogenization of the density parameters, called the Solid Isotropic Material with Penalization method (SIMP), introduced by Bendsøe and Sigmund [20]. Noticeable examples are the open-source optimization repository MetaNet [21] and Machine Learning (ML)-aided optimization tools [22, 23]. To our knowledge, the state-of-the-art performance of manufactured broadband blazed metasurface gratings designed with TO is around 55% of average efficiency for 5 wavelengths between 900 nm and 1,300 nm, for both polarizations (different grating for TE and TM) [24]. Another design, solely based on the phase shift induced by blazed gratings [25], has demonstrated the same performance on the wavelength range [350–1,100] nm. There are some recent works in the IR with very high broadband performances, such as in Ref. [26]. However the targeted wavelength range of [6–12] μm in this study is actually an octave, with the same energy gap as the [400–800] nm visible range. Such broadband studies in the Vis/NIR region are not common.

This is why we have recently developed an open-source, bespoke, FEM-based and large-parameter topology optimization tool that addressed the issue of nanostructured blazed gratings for the Vis/NIR

range [400–1,500] nm [27], based on Python and the Gmsh/GetDP software suite [28, 29]. It can find an optimal design on any wavelength range, on any diffraction order, with any pair of materials under conical incidence, *i.e.* mono-periodic (or 1D) grating with a free incidence. We had demonstrated a silica design with an average efficiency of 81% on these two octaves, hence 56% higher than the current sawtooth-profiled gratings (52%) in relative terms. Its manufacturability was however compromised, since it contained levitating elements and highly challenging elementary patterns. Dual material gratings ensuring mechanical sustainability had been tested with the same solver [30]. The performances were unfortunately degraded, while the fabrication remained highly challenging.

This article deals with the improvement of our open-source design solver, generalized in 3D and adapted to manufacturability constraints established in Ref. [31]. Particularly, we present a manufacturable metasurface made of elementary pillars that outperforms the current broadband propositions on the two octaves [400–1,500] nm. The theoretical general background of bi-periodic (or 2D) gratings is reminded in Section 2. The TO problem and its resolution using the adjoint method is exposed in Section 3. The two improvements developed on our optimization tool are presented in Section 4. The 3D mesh-based solver is described in Section 5 and the pillar-based solver in Section 6. Conclusion and perspectives are led in Section 7. The code in the conical/3D mesh-based and 3D pillar-based frameworks is totally open source and available in the [Code File](#). The comparison between the conical and the 3D mesh-based solvers, completing Section 5, is enhanced in [Appendix](#).

2 Choice of the Geometry and Paradigm Change in 3D

2.1 Problem Description

The device that deflects each wavelength inside a spectrograph is the *diffraction grating*. It is a periodic structure, exhibiting a density of tens to several thousands of lines per millimeter for visible and NIR optics. Depending on the instrument, diffraction can occur either in transmission or in reflection.

If nothing special is done to the shape of the grating, diffraction occurs in many orders. However, to obtain scientifically usable images – that is, to reach a desired SNR – a maximum flux on a single *diffraction order* is preferred. Gratings that achieve this are known as *blazed gratings* and the traditional sawtooth profile is illustrated in Fig. 1.

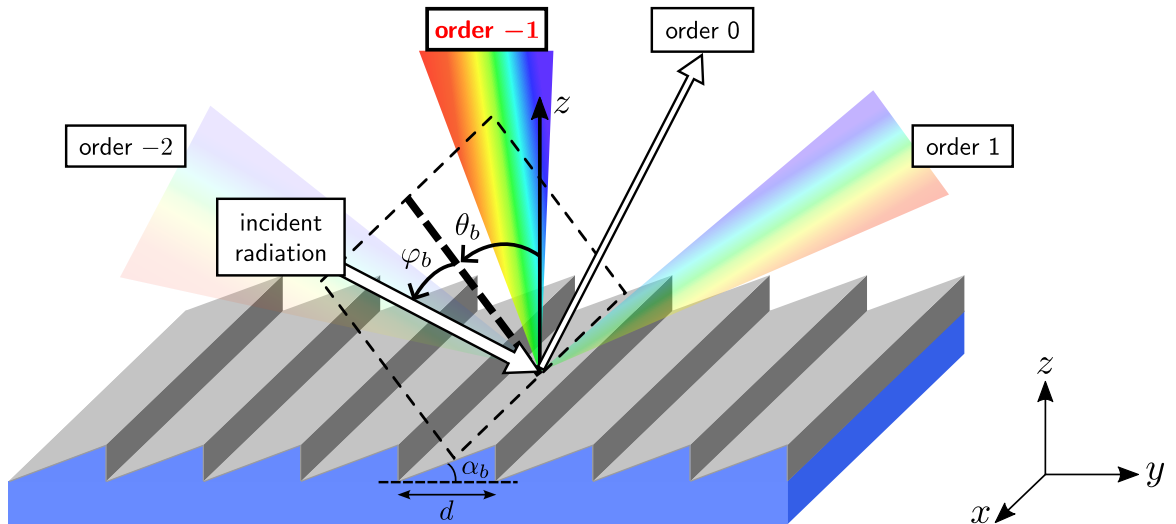


Figure 1: The blazing effect of a sawtooth grating in reflection, with a white light incident radiation. The diffraction phenomenon is illustrated with 4 diffraction orders: -2 , -1 , 0 and 1 . The grating is blazed, *i.e.* most part of the diffracted light is on a specific order (here the -1 st).

The goal remains the same as in Ref. [27]: use the high versatility of the metasurface to optimize its pattern. On the one hand, the sawtooth grating reminded in Fig. 2a has no much room for improvement. Changing the combination of the *blaze angle* α_b and the period d_y only changes the targeted wavelength range and diffraction order. On the other hand, the bi-periodic or 2D metasurface configuration sketched in Fig. 2b (here with a *binary grating* composed of dielectric pillars) demonstrates a wide range of optimizable parameters – layer thickness, pillar dimensions, material. As the number of optimization Degrees of Freedom (opt. DoFs) is large and to keep the same mesh during the whole process, TO is chosen.

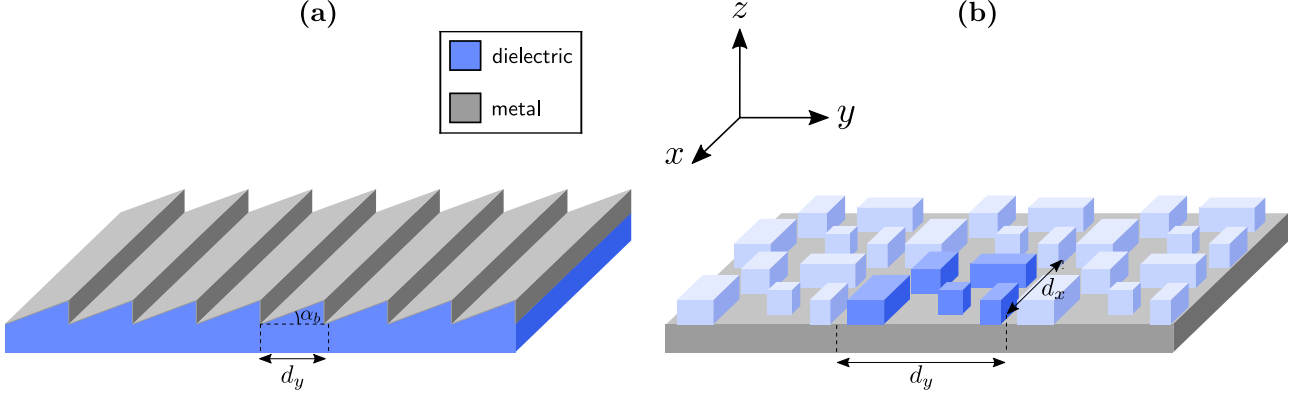


Figure 2: (a) The reference sawtooth blazed grating. It is mono-periodic or 1D with a period denoted d_y and the so-called blaze angle α_b . (b) Pillar-shaped bi-periodic (or 2D) metasurface grating. One period of the pattern is highlighted with a darker color; its surface is $d_x \times d_y$.

A more general definition of bi-periodic gratings is given in the next subsection. It is inspired from the SIMP interpolation method of the relative permittivity within the design region, enabling for a freeform optimized pattern.

2.2 Computational Domain in 3D

A point in the domain is denoted $\mathbf{x} = (x, y, z) \in \mathbb{R}^3$. The structure and numerical domain are comparable to 2D as illustrated in Fig. 3. One finds from top to bottom: the top Perfectly Matched Layer (PML⁺), absorbing the outgoing waves; the superstrate \mathcal{S}^+ ; the design region Ω_d ; the substrate \mathcal{S}^- ; the bottom PML PML⁻, not necessary for problems in reflection. However, every sub-domain is now parallelepipedic. As a consequence, the interfaces of interest are now surfaces. For reflected (respectively (resp.) transmitted) diffracted fields, we study the interface Γ^+ highlighted in red between \mathcal{S}^+ and PML⁺ (resp. Γ^- between \mathcal{S}^- and PML⁻).

Remark: Compared to the conical case, the 3D axes are changed: the (Oz) axis is now normal to the design region. Therefore, the main period of the grating is along the (Oy) axis and is thus denoted d_y ; the grating lines are along the (Ox) axis and the subwavelength period is thus denoted d_x . This nuance is important to note, as the [Code File](#) follows the same convention.

The grating is illuminated by an incident linearly polarized plane wave \mathbf{E}^{inc} with a free-space wavelength λ (frequency f , angular frequency ω). The angles of incidence $\theta_i \in [0, \pi/2[$, $\varphi_i \in]-\pi, \pi]$ define its wavevector \mathbf{k}_\downarrow^+ in spherical coordinates. The explicit definition of \mathbf{k}_\downarrow^+ is given later in the next subsection. The polarization basis vectors $\hat{\mathbf{s}}$ and $\hat{\mathbf{p}}$ are defined such as $(\hat{\mathbf{p}}, \hat{\mathbf{s}}, \mathbf{k}_\downarrow^+/k^+)$ is an orthonormal basis ($k^+ := |\mathbf{k}_\downarrow^+|$) and $\hat{\mathbf{s}}$ is parallel to the (Oxy) plane. The polarization angle ψ_i , between $\hat{\mathbf{s}}$ and \mathbf{E}^{inc} , completes the definition of the latter.

Let $\rho : \Omega_d \ni \mathbf{x} \mapsto \rho(\mathbf{x}) \in [0, 1]$ be a density field in the design region and let $\mathbf{x} \in \Omega_d$ be a given point in this same region. The relative permittivity at this position is defined using the SIMP method,

which is the following bijection:

$$\varepsilon_r^d(\lambda, \mathbf{x}) = (\varepsilon_{r,2}(\lambda) - \varepsilon_{r,1}(\lambda))\rho(\mathbf{x}) + \varepsilon_{r,1}(\lambda) \quad (1)$$

where $\varepsilon_{r,1}$ and $\varepsilon_{r,2}$ are resp. the minimal and maximal relative permittivity in Ω_d . Note that if one desires a complex refractive index within the design region – e.g., a metal or silicon for UV/Vis light – a non-linear interpolation scheme demonstrates better convergence capabilities [32, 27].

There exists two main ways to describe the response of the grating through PDEs in the harmonic regime, for a plane wave and distant source. Both rely on the *Helmholtz Propagation Equation*, but one chooses between a total or a scattered field description. The second one is selected here, and we refer the reader to Ref. [27] for the detailed calculations to obtain it, using the annex (or ancillary) field \mathbf{E}_a . The next section only adapts it to the 3D notations.

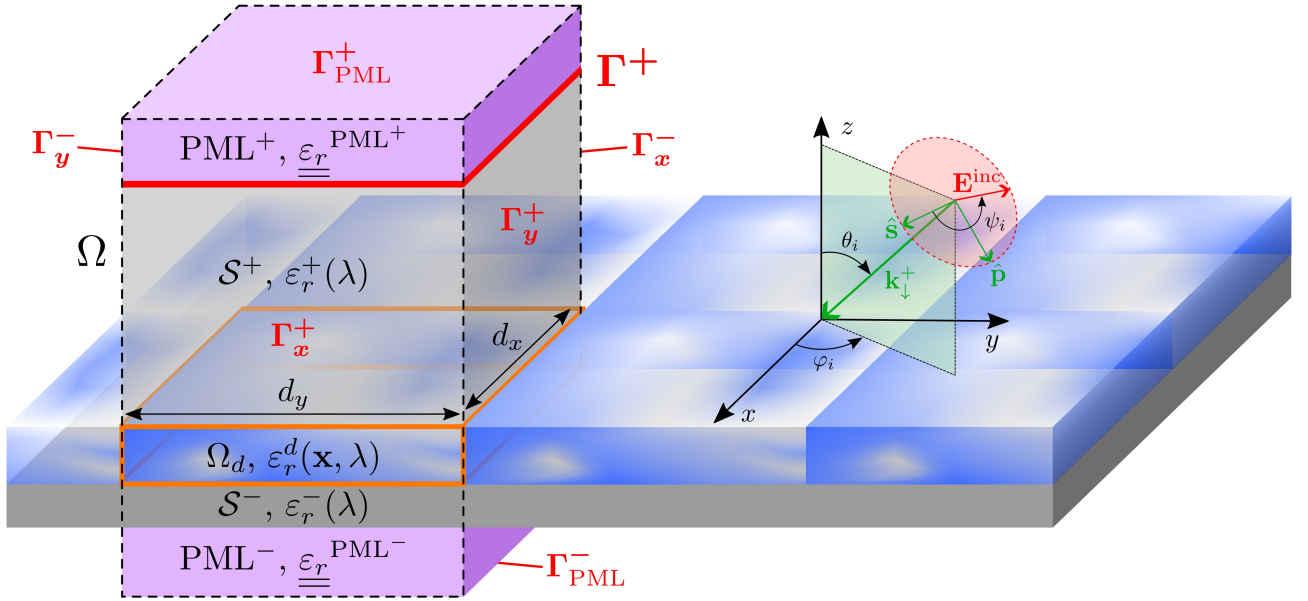


Figure 3: Description of the numerical domain for a bi-periodic grating and definition of the incident electric field. In every domain, the permittivity tensor is defined. The region of interest (where the metasurface lies) is the design region Ω_d (surrounded by the orange cuboid). The material where the incident radiation travels is the superstrate \mathcal{S}^+ (in transparent gray). The reflecting metallic layer is the substrate denoted \mathcal{S}^- (in gray). The surface on top of \mathcal{S}^+ is the interface where the diffracted field is analyzed, called Γ^+ (in red). The periodicity of the pattern enables to restrain the domain to a sole $d_x \times d_y$ period, with absorbing Perfectly Matched Layers up and down (PML^\pm , in violet). The incident electric field is perpendicular to the direction of propagation given by the vector \mathbf{k}_\downarrow^+ . It is defined by the polar angle θ_i , the azimuthal angle φ_i and the polarization angle ψ_i .

2.3 The Scattered Field Formulation in 3D

The incident field is defined as $\mathbf{E}^{\text{inc}} = \mathbf{A}_e \exp(i\mathbf{k}_\downarrow^+ \cdot \mathbf{x})$, $\forall \mathbf{x} \in \mathbb{R}^3$, where [4]

$$\mathbf{k}_\downarrow^+ = \begin{pmatrix} k_x \\ k_y \\ k_z^+ \end{pmatrix} = k^+ \begin{pmatrix} -\sin \theta_i \cos \varphi_i \\ -\sin \theta_i \sin \varphi_i \\ -\cos \theta_i \end{pmatrix}, \quad (2)$$

denoting $k^+ = k_0 \sqrt{\varepsilon_r^+ \mu_r^+}$ with $k_0 = 2\pi/\lambda$. The vector amplitude writes

$$\mathbf{A}_e = A_e \begin{pmatrix} \cos \psi_i \cos \theta_i \cos \varphi_i - \sin \psi_i \sin \varphi_i \\ \cos \psi_i \cos \theta_i \sin \varphi_i + \sin \psi_i \cos \varphi_i \\ -\cos \psi_i \sin \theta_i \end{pmatrix}. \quad (3)$$

We look for the scattered field \mathbf{E}_*^d , sum of all the outgoing fields of the problem induced by the grating. As a consequence of the Floquet-Bloch theorem, the response of a bi-periodic grating to a plane incident wave is a bi-quasi-periodic wave, *i.e.*, a field \mathbf{U} such that

$$\forall \mathbf{x} \in \mathbb{R}^3, \quad \mathbf{U}(x, y, z) = \mathbf{U}^\#(x, y, z) e^{ik_x x} e^{ik_y y} \quad (4)$$

where $\mathbf{U}^\#$ is a bi-periodic function with periods d_x along x and d_y along y . The boundary condition $\mathbf{E}_*^d(\Gamma_{\{x,y\}}^+) = e^{ik_{\{x,y\}} d_{\{x,y\}}} \mathbf{E}_*^d(\Gamma_{\{x,y\}}^-)$ is therefore settled.

In addition, if the PMLs have a sufficient thickness, the field can be safely neglected on their end (at the maximal $|z|$). By "sufficient thickness", we mean a distance for which $|\mathbf{E}_*^d| \ll |\mathbf{E}^{\text{inc}}|$ at the PML's end. Typically, $2\lambda_{\text{min}}$ is satisfactory enough, with in our case $|\mathbf{E}_*^d| \simeq 10^{-5} |\mathbf{E}^{\text{inc}}|$. A tangential Dirichlet condition is therefore settled on the upper and lower boundaries to reduce the number of FEM unknowns:

$$\mathbf{E}_*^d \times \hat{\mathbf{z}} = 0 \text{ in } \Gamma_{\text{PML}}^\pm. \quad (5)$$

Let $\mathcal{V} := \mathcal{H}_0(\mathbf{curl}, \Omega, k_x d_x, k_y d_y)$ be the computation set with these boundary conditions – 0 designating tangential Dirichlet and $k_x d_x, k_y d_y$ the bi-quasi-periodicity. The scattered field formulation of the Helmholtz propagation equation remains the same as under conical incidence:

Find $\mathbf{E}_*^d \in \mathcal{V}$ such that for all $\mathbf{x} \in \mathbb{R}^3$ with $\omega \in \mathbb{R}^+$,

$$\mathbf{curl} \left(\underline{\underline{\mu_r}}^{-1} \mathbf{curl} \mathbf{E}_*^d \right) - k_0^2 \underline{\underline{\varepsilon_r}} \mathbf{E}_*^d = k_0^2 \left(\underline{\underline{\varepsilon_r}} - \underline{\underline{\varepsilon_r^a}} \right) \mathbf{E}_a. \quad (6)$$

However, its weak formulation is formally much simpler in 3D since there is no distinction between the longitudinal and tangential components of the field:

Find $\mathbf{E}_*^d \in \mathcal{V}$ such that for all $\mathbf{E}' \in \mathcal{V}$,

$$\int_{\Omega} \left[\underline{\underline{\mu_r}}^{-1} \mathbf{curl} \mathbf{E}_*^d \cdot \mathbf{curl} \overline{\mathbf{E}'} - k_0^2 \left(\underline{\underline{\varepsilon_r}} \mathbf{E}_*^d - (\underline{\underline{\varepsilon_r^a}} - \underline{\underline{\varepsilon_r}}) \mathbf{E}_a \right) \cdot \overline{\mathbf{E}'} \right] d\Omega = 0. \quad (7)$$

Another consequence changing from the mono-periodic case is that there are $N_r \times M_r$ existing diffraction orders in reflection (resp. $N_t \times M_t$ in transmission). The components of the wave vectors for each diffraction order in reflection $(n, m) \in \{(n, m) \in \mathbb{Z}^2 / k_{z,n,m}^+ \in \mathbb{R}\}$ (resp. $k_{z,n,m}^- \in \mathbb{R}$ in transmission) are then:

$$\begin{cases} k_{x,n} &= k_x + \frac{2\pi}{d_x} n \\ k_{y,m} &= k_y + \frac{2\pi}{d_y} m \\ k_{z,n,m}^+ &= -\sqrt{k_0^2 \varepsilon_r^+ - k_{x,n}^2 - k_{y,m}^2} \\ k_{z,n,m}^- &= -\sqrt{k_0^2 \varepsilon_r^- - k_{x,n}^2 - k_{y,m}^2} \end{cases}. \quad (8)$$

The so-called complex amplitudes in reflection $r_{n,m}^u$ and in transmission $t_{n,m}^u$ ($u \in \{x, y\}$), coming from the Fourier decomposition, write

$$\begin{cases} r_{n,m}^u = \frac{1}{d_x d_y} \int_{\Gamma^+} e^{-i(k_{x,n} x + k_{y,m} y)} \mathbf{E}^d(x, y, z_0) \cdot \hat{\mathbf{u}} dx dy & \text{for } z_0 > z_{\Omega_d} \\ t_{n,m}^u = \frac{1}{d_x d_y} \int_{\Gamma^-} e^{-i(k_{x,n} x + k_{y,m} y)} \mathbf{E}^{\text{tot}}(x, y, z_0) \cdot \hat{\mathbf{u}} dx dy & \text{for } z_0 < 0 \end{cases}. \quad (9)$$

Finally the diffraction efficiencies are computed using the formula in Ref. [33], using only the continuous components of the field – *i.e.*, tangential to the interfaces, hence along x and y :

$$\begin{cases} R_{n,m} = \frac{1}{k_{z,n,m}^+ k_z^+ A_e^2} \left[(k_{x,n}^2 + (k_{z,n,m}^+)^2) |r_{n,m}^x|^2 \right. \\ \quad \left. + (k_{y,m}^2 + (k_{z,n,m}^+)^2) |r_{n,m}^y|^2 \right. \\ \quad \left. + 2k_{x,n} k_{y,m} \operatorname{Re}(r_{n,m}^y \overline{r_{n,m}^x}) \right] \\ T_{n,m} = \frac{1}{k_{z,n,m}^- k_z^+ A_e^2} \left[(k_{x,n}^2 + (k_{z,n,m}^-)^2) |r_{n,m}^x|^2 \right. \\ \quad \left. + (k_{y,m}^2 + (k_{z,n,m}^-)^2) |r_{n,m}^y|^2 \right. \\ \quad \left. + 2k_{x,n} k_{y,m} \operatorname{Re}(r_{n,m}^y \overline{r_{n,m}^x}) \right] \end{cases}. \quad (10)$$

Our goal is to optimize the reflection efficiency $R_{0,-1}$, which is equivalent to R_{-1} in a 2D or conical incidence. Note that in practice, the period d_x is voluntarily taken subwavelength to prevent diffraction on the orders $n \neq 0$. This second periodicity only allows for more freedom in the optimal design.

3 Optimization Problem and Adjoint Method

3.1 Merit Function and its Jacobian

Let \mathfrak{T} be the triangulation obtained using the FEM. There is a finite number \mathcal{N}_T of tetrahedra in the design region Ω_d . Let then $\mathcal{T}_i \in \mathfrak{T}|_{\Omega_d}$, $i \in \{1, \dots, \mathcal{N}_T\}$ be one of these tetrahedra. The relative permittivity is defined per mesh element, meaning that in Eq. (1), $\forall \mathbf{x} \in \mathcal{T}_i$, $\rho(\mathbf{x}) = \rho_i$, with ρ_i a constant real number between 0 and 1. The opt. DoFs are the densities ρ_i into the design region, and $\boldsymbol{\rho} = (\rho_1, \dots, \rho_{\mathcal{N}_T})$ is called the *design variable*.

A connectedness filter $\boldsymbol{\rho}_f$ [34] and a binarization filter $\hat{\boldsymbol{\rho}}$ [35] are applied. The filtered design variable writes then

$$\hat{\boldsymbol{\rho}}_f : [0, 1]^{\mathcal{N}_T} \ni \boldsymbol{\rho} \mapsto (\hat{\boldsymbol{\rho}} \circ \boldsymbol{\rho}_f)(\boldsymbol{\rho}) \in [0, 1]^{\mathcal{N}_T}. \quad (11)$$

We denote by $\mathcal{R}_{n,m}$ the reflection efficiency on the order (n, m) of the structure obtained using the filtered design variable: $\mathcal{R}_{n,m} : [0, 1]^{\mathcal{N}_T} \ni \boldsymbol{\rho} \mapsto (R_n \circ \hat{\boldsymbol{\rho}} \circ \boldsymbol{\rho}_f)(\boldsymbol{\rho}) \in [0, 1]$. The optimization problem is then to minimize the merit function $\mathcal{F}_{n,m} := 1 - \mathcal{R}_{n,m}$. The optimization problem writes:

$$\begin{aligned} \min_{\boldsymbol{\rho}} \quad & \mathcal{F}_{n,m}(\boldsymbol{\rho}) \\ \text{such that} \quad & \begin{cases} \mathcal{L}(\boldsymbol{\rho}, \mathbf{E}') = 0 & \forall \mathbf{E}' \in \mathcal{V} \\ 0 \leq \rho_i \leq 1 & \forall i \in \{1, \dots, \mathcal{N}_T\} \end{cases}, \end{aligned} \quad (12)$$

where \mathcal{L} designates the weak formulation in Eq. (7), that is:

$$\begin{aligned} \mathcal{L} : \mathbb{R}^{\mathcal{N}_T} \times \mathcal{V} \ni (\boldsymbol{\rho}, \mathbf{E}') \mapsto \int_{\Omega} \left[\underline{\underline{\mu_r}}^{-1} \operatorname{curl} \mathbf{E}_*^d(\boldsymbol{\rho}) \cdot \operatorname{curl} \overline{\mathbf{E}'} \right. \\ \left. - k_0^2 \left(\underline{\underline{\varepsilon_r}}(\boldsymbol{\rho}) \mathbf{E}_*^d(\boldsymbol{\rho}) + (\underline{\underline{\varepsilon_r}}(\boldsymbol{\rho}) - \underline{\underline{\varepsilon_{r,a}}}) \mathbf{E}_a \right) \cdot \overline{\mathbf{E}'} \right] d\Omega \in \mathbb{R}. \end{aligned} \quad (13)$$

Using the chain rule, the Jacobian of the merit function of Problem (12) is:

$$\frac{\partial \mathcal{F}_{n,m}}{\partial \boldsymbol{\rho}}(\boldsymbol{\rho}) = \frac{\partial \boldsymbol{\rho}_f}{\partial \boldsymbol{\rho}}(\boldsymbol{\rho}) \frac{\partial \hat{\boldsymbol{\rho}}_f}{\partial \boldsymbol{\rho}_f}(\boldsymbol{\rho}_f) \frac{\partial \mathcal{F}_{n,m}}{\partial \hat{\boldsymbol{\rho}}_f}(\hat{\boldsymbol{\rho}}_f). \quad (14)$$

The differentiation of the first line in Eq. (10) leads to, for all $i \in \{1, \dots, \mathcal{N}_T\}$:

$$\begin{aligned} \frac{\partial F_{n,m}}{\partial \hat{\rho}_{f,i}} = -\frac{\partial R_{n,m}}{\partial \hat{\rho}_{f,i}} = & -\frac{2}{k_{z,n,m}^+ k_z^+ A_e^2} \operatorname{Re} \left[(k_{x,n}^2 + (k_{z,n,m}^+)^2) \frac{\partial r_{n,m}^x \overline{r_{n,m}^x}}{\partial \hat{\rho}_{f,i}} \right. \\ & + (k_{y,m}^2 + (k_{z,n,m}^+)^2) \frac{\partial r_{n,m}^y \overline{r_{n,m}^y}}{\partial \hat{\rho}_{f,i}} \\ & \left. + k_{x,n} k_{y,m} \left(\frac{\partial r_{n,m}^y \overline{r_{n,m}^x}}{\partial \hat{\rho}_{f,i}} + r_{n,m}^y \frac{\partial \overline{r_{n,m}^x}}{\partial \hat{\rho}_{f,i}} \right) \right]. \end{aligned} \quad (15)$$

3.2 The adjoint problem to access the derivatives of the complex amplitudes

Let (n, m) be the targeted diffraction order to maximize. The derivatives of $r_{n,m}^u$ with respect to the $\hat{\rho}_{f,i}$, $i \in \{1, \dots, \mathcal{N}_T\}$, around the equilibrium point $\hat{\rho}_{f,*}$ are given by

$$\frac{\partial r_{n,m}^u}{\partial \hat{\rho}_{f,i}}(\hat{\rho}_{f,*}) = \int_{\mathcal{T}_i} k_0^2 (\varepsilon_{r,2} - \varepsilon_{r,1}) \mathbf{E}^{\text{tot}}(\boldsymbol{\rho}_*) \cdot \boldsymbol{\lambda}_{*,n,m}^u \, d\Omega, \quad (16)$$

where $\mathcal{T}_i \in \mathfrak{T}_{|\Omega_d}$ is the tetrahedron of the mesh element in the design region with the density $\hat{\rho}_{f,i}$, and $\boldsymbol{\lambda}_*^u$ is the unique solution of the adjoint problem, noting $\mathcal{V}^{\text{adj}} = \mathcal{H}_0(\mathbf{curl}, \Omega, e^{-\iota k_x x}, e^{-\iota k_y y})$:

Find $\boldsymbol{\lambda}_{*,n,m}^u \in \mathcal{V}^{\text{adj}}$ such that for all $\boldsymbol{\lambda}' \in \mathcal{V}^{\text{adj}}$,

$$\int_{\Omega} \left[\underline{\underline{\mu}}_r^{-1} \mathbf{curl} \boldsymbol{\lambda}_{*,n,m}^u \cdot \mathbf{curl} \overline{\boldsymbol{\lambda}'} - k_0^2 \underline{\underline{\varepsilon}}_r \boldsymbol{\lambda}_{*,n,m}^u \cdot \overline{\boldsymbol{\lambda}'} \right] d\Omega = \frac{1}{d_x d_y} \int_{\Gamma^+} e^{-\iota k_x n x} e^{-\iota k_y n y} \hat{\mathbf{u}} \cdot \overline{\boldsymbol{\lambda}'} \, d\Gamma. \quad (17)$$

This result enables to compute the Jacobian of the merit function. A demonstration of this property is available in Ref. [27] in the conical case. Basically, it is the same in 3D, with this formally more compact weak formulation.

4 Two ways of defining the density distribution

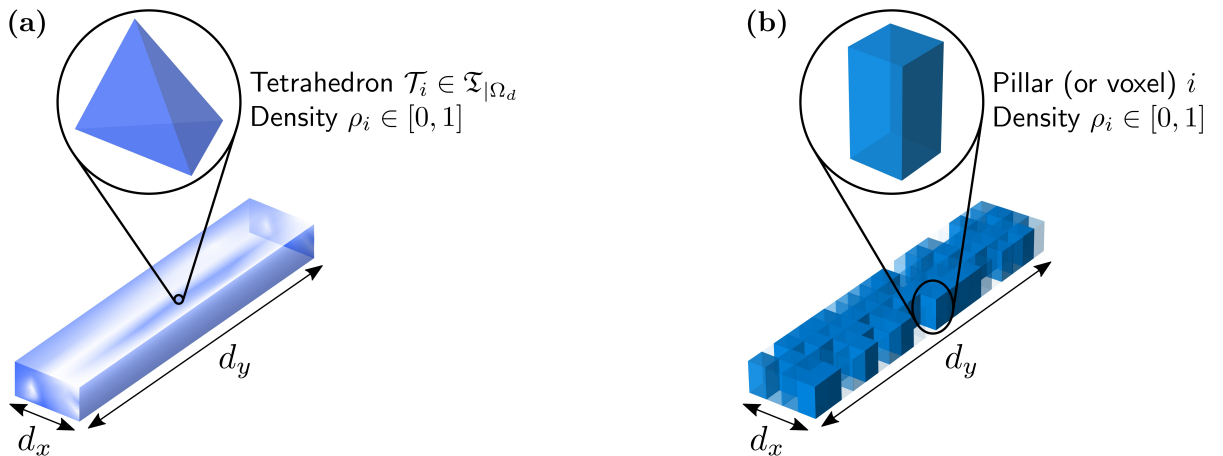


Figure 4: (a) Mesh-based density distribution. Every tetrahedron $\mathcal{T}_i \in \mathfrak{T}_{|\Omega_d}$ has got a density ρ_i that is optimized. It can be seen as a freeform optimization (a tetrahedron is very small compared to the pattern size). (b) Pillar-based density distribution. Same principle but the density is defined by cuboids that have a manufacturable size.

For our study, the period d_x is considered sub-wavelength to avoid the diffraction along the grating lines (the orders corresponding to n in $R_{n,m}$). A period of the grating looks therefore like in Fig. 4, with $d_y \sim 10d_x$.

We present hereby two ways to define the density distribution using the SIMP. The first fixes the support of every ρ_i on a tetrahedron of the FE mesh, as illustrated in Fig. 4a. The second defines ρ_i on a manufacturable cuboid, like in Fig. 4b. By "manufacturable", we mean that the dimensions of the elementary elements have been proven to be fabricated using nanofabrication techniques such as electron-beam (or more commonly e-beam) lithography for the patterning and Reactive Ion Etching (RIE) [36].

5 Mesh-Based Topology Optimization

The optimization on the 3D pattern is performed in a 600 nm-thick design region with $d_y = 3,300$ nm and $d_x = 330$ nm, using a set of 17 wavelengths between $\lambda = 400$ nm and $\lambda = 1,500$ nm, with higher density in the visible spectrum (see the targeted wavelengths represented by the green dots in Fig. 5c). The material is SiO_2 and the incident angles are $\theta_i = 24.5^\circ$, $\varphi_i = -11^\circ$ with an s -polarization $\psi_i = 0^\circ$. The 47,791 opt. DoFs problem is launched on 17 threads for the wavelengths and 2 threads per wavelength for the FE matrix inversion, on a workstation equipped with a 64-core CPU and 4Tb of RAM. The optimization process took 10 days for 882 iterations, with peaks of RAM utilization at 1.2Tb.

The optimal pattern is shown with two points of view in Figs. 5a–b. The first view separates the three Cartesian axes to provide a clear view of the structure's geometry and illustrates the dimensions of the pattern's period. The second view reproduces the point of view for 2D cases (on the $x = d_x$ plane) to highlight the striking resemblance between this 3D profile and that of the optimal design in the conical case for the same specifications (see Appendix). Although this 3D structure exhibits a variation of shape along the x axis, the similarity is confirmed with the spectral response of both patterns in Fig. 5c. The blue and gray lines correspond resp. to the spectral response of the 3D and the conical grating on the -1 st diffraction order. The gap between them remains very narrow across the whole spectral range, and their average efficiency is actually the same (62%).

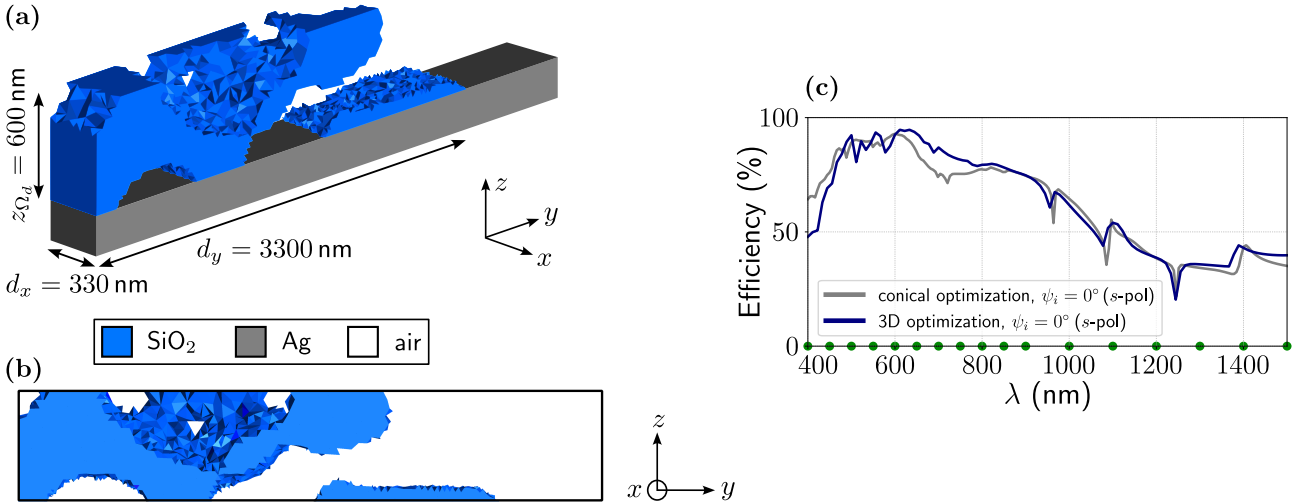


Figure 5: (a) 3D view of the optimal 3D pattern on a single period for a 600 nm-thick design region with SiO_2 as chosen dielectric. (b) Same pattern viewed on the plane $x = d_x$ (similar to the point of view of 2D gratings). (c) Spectral response of the grating on the wavelength range of interest (blue line) as compared to the response for the targeted incidence of the conical optimal design (gray line).

The benefit of the 3D optimization is that the polarization dependence is significantly diminished with respect to the conical case (see [Appendix](#)). The absolute average difference between both polarizations on the 2 octaves is only 7% – the strong blazing effect is more polarization-independent. This result remains surprising, as we would expect a superior local optimum given all the possibilities enabled by the new 3rd dimension. Another improvement in this optimal pattern is its better mechanical sustainability. Even if this pattern is difficult to manufacture, there is at least no levitating isolated elements.

The 3D mesh-based, topology-optimized grating is not the expected ultimate design for high-efficiency blazing. Perhaps the roughness imposed by the mesh tetrahedra – more important in 3D as these elements are bigger than in the conical case to limit computation burden – is one of the causes of this lack of improvement envisioned from the addition of a new dimension. We could also see this result conversely: maybe the conical case already encompasses the best optima for mesh-based distributions.

Topology optimization on bi-periodic structures is absolutely not abandoned, however. If we can see the optimal pattern in the conical case as a maximal threshold for mesh-based gratings, other discretizations of the design variable ρ could bypass the strong roughness observed here and maybe provide equivalent, or even better performance. To settle a framework for these other distributions, the manufacturability of the grating becomes of primary interest.

6 Pillar-Based Topology Optimization

6.1 From the mesh to the voxels

Commonly, topology optimization is seen as a method yielding a pattern with a shape left free inside the design region. It is the case for the mesh-based distribution of relative permittivity (Fig. 4a) since the mesh elements are small with respect to the filter radius $r_f = 300$ nm. However, the method itself can be applied to discrete density distributions other than the FE mesh elements. As motivated by the metasurface fabrication, we now choose to rely on manufacturable cuboids as illustrated in Fig. 4b. Note that these cuboids are larger than the typical mesh size, yet they remain smaller than the wavelength, preventing from getting sharp resonances inside a single voxel. In other words, increasing the voxel size too much could lead to poorer convergence of the adjoint method.

A convergence test is thus provided, based on a numerical domain of $200 \times 1,000 \times 600$ nm. While this optimization method still relies on a 3D model, the number of opt. DoFs is significantly lower. Therefore, testing the adjoint method on every pillar without excessive processing time is possible.

Let us then define a random permittivity function, constant per pillar in a 3×15 pillar configuration and incident angles of $\theta_i = 24.5^\circ$, $\varphi_i = -11^\circ$ and $\psi_i = 0^\circ$ (*s*-polarization). This random permittivity function is kept the same for every mesh size and is shown in Fig. 6a. We represent in Fig. 6b the minimum and maximum values (orange solid lines) of the relative difference between the adjoint-based and the finite-difference-based computations of the Jacobian of the merit function, in \log_{10} scales. The mean values of the relative differences on the 45 pillars are linearly fitted starting from $r_T = \lambda/14$. It leads to a gradient of -1.5 , which highlights an average gain of 1.5 significant digits on the accuracy of the adjoint method when the tetrahedron size is divided by 10.

In conclusion, the pillar-based optimization can still rely on the adjoint method. The tetrahedron size is taken as $r_T = \lambda_{\min}/14$ to reduce the computational burden while maintaining satisfactory precision. All the manufacturability constraints introduced in this chapter are gathered in the next subsection to provide a pattern that can be etched using e-beam lithography and RIE.

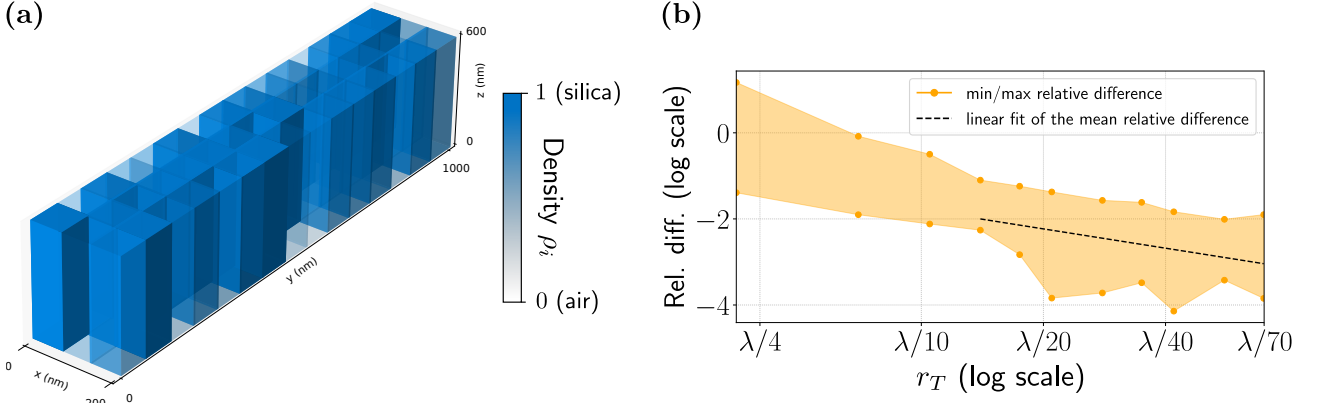


Figure 6: Convergence test of the adjoint method on the pillar-based grating, for random permittivities distributed on 45 squared pillars, on a $200 \times 1,000 \times 600$ nm period, for the wavelength $\lambda = 700$ nm and incident angles $\theta_i = 24.5^\circ$, $\varphi_i = -11^\circ$ and $\psi_i = 0^\circ$. **(a)** Pillar-based random distribution obtained and set for the convergence test, with relative permittivities between 0 (air) and 1 (silica) **(b)** Minimum and maximum values (orange solid lines) taken by the relative differences between the adjoint-based and the finite-difference-based computations of the Jacobian of the merit function, delimiting the orange-colored region where all the relative values lie. Their mean value is linearly fitted (dashed black line) starting from $r_T = \lambda/14$.

6.2 Manufacturable Metasurface Designed With Topology Optimization

In standard manufacturing processes including e-beam lithography and RIE, the deposition of an etch stop layer protecting the silver substrate must be taken into account. A 50 nm-thick of alumina Al_2O_3 is therefore added in the numerical domain and for the optimization process. The period of $330 \times 3,300$ nm is divided into 4×40 squared pillars, which leads to edges of 82.5 nm. The dielectric is Si_3N_4 with a thickness of $z_{\Omega_d} = 200$ nm, yielding an aspect ratio of 2.7 which is achievable (see for instance the silica pattern in Ref. [25] with a ratio aspect of 3 and 600 nm-thickness). The set of targeted wavelengths is $\Lambda = \{400, 500, 600, \dots, 1,500\}$ nm. The incident angles are still $\theta_i = 24.5^\circ$, $\varphi_i = -11^\circ$ and s-polarization $\psi_i = 0^\circ$.

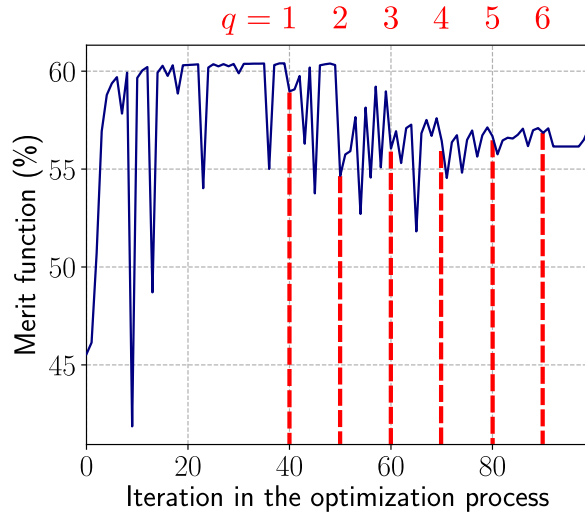


Figure 7: Convergence during the optimization process for a 200 nm-thick, 4×40 pillar pattern made of Si_3N_4 on a 50 nm-thick layer of alumina. The binarization steps, identified by the binarization factor q (in red), are highlighted by the dashed red lines.

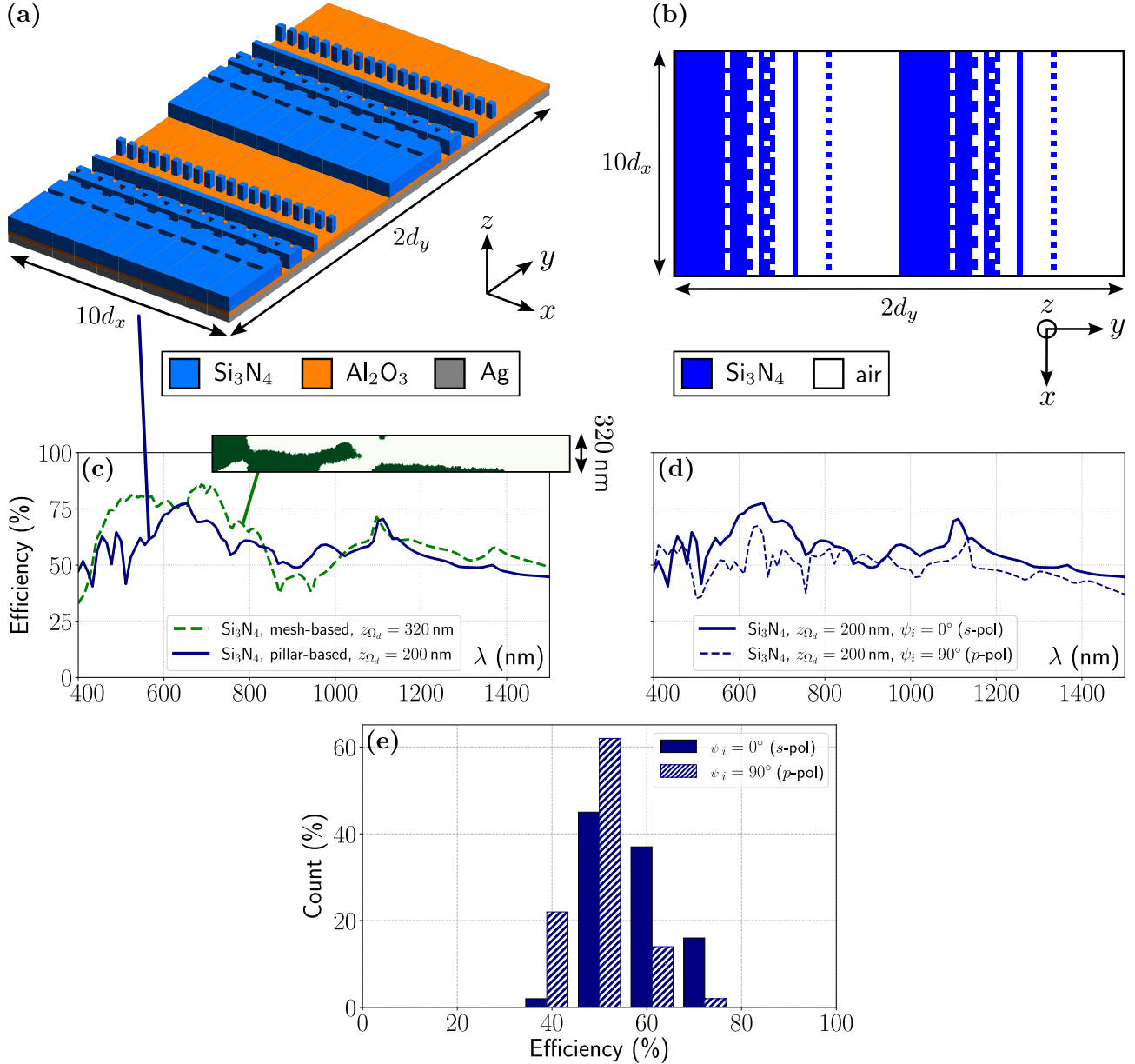


Figure 8: (a) 3D view of 10×2 periods of the 200 nm-thick Si₃N₄ optimal pattern. (b) View from above of the same cell. Only Si₃N₄ (in blue) is represented. (c) Spectral response on the diffraction order -1 of this pattern (solid blue line) as compared to that of the mesh-based 320 nm-thick pattern under conical incidence (pattern in green, spectral response in dashed green line). (d) Polarization dependence of the optimal pillar pattern for the s -polarization $\psi_i = 0^\circ$ (solid line) and p -polarization $\psi_i = 90^\circ$ (dashed line). (e) Efficiency breakdown of the structure (in percentage) for both polarization cases (solid bars: s -polarization and hatched bars: p -polarization).

Reducing the number of opt. DoFs to only 160 is of great interest in 3D. The convergence is much faster and one can settle a lower number of maximum iterations. Therefore, this optimization only takes 14 h 50 min to run 100 iterations, parallelized on wavelengths with 4 threads per wavelength (therefore 48 threads in total). The iteration history is shown in Fig. 7 to illustrate that the algorithm almost immediately reaches the local maximum of the objective function, long before the changeover to the binarization step $q = 1$ at the iteration 40 (first dashed vertical red line). The merit function remains quite constant afterwards, without depending on the increasing binarization. This is why the

q binarization parameter changeover is imposed only every 10 iterations (other dashed vertical red lines).

The optimized pattern obtained is shown on 2 main periods (along the y axis) and 10 periods along the gratings lines (x axis) in Fig. 8a (3D view) and Fig. 8b (view from above) with the associated spectral response in blue line in Fig. 8c. The latter’s primal quality is its steadiness above 50% on both octaves without forbidden wavelengths, which is preferable even if the average efficiency is now 57%. Furthermore, the polarization dependence is restrained, with the average efficiency for p -polarization $\psi_i = 90^\circ$ at 50% (Fig. 8d). The unpolarized uniformity of the response is endorsed by the efficiency distribution histogram in Fig. 8e. The whole spectrum is reflected with an efficiency between 35 and 75%, 80% of the wavelengths being concentrated in a 20%-interval ([45–65]% for s -polarization and [35–55]% for p -polarization).

This grating satisfies a large number of performance and manufacturability criteria, which makes it the best candidate for the next blazed metasurface device to be fabricated. Allowing for a blazing effect on such a wide band inevitably implies for the optimal pattern to avoid any material in the right zone of the period along the y axis, *i.e.* a large hole of a bit less than $1\ \mu\text{m}$. This remains a sensitive technical aspect for the fabrication, but it is not impossible.

In this final section, we have linked the manufacturing capabilities of e-beam lithography and RIE for nanostructures with our optimization code, providing a broadband blazed metasurface on two octaves which fabrication is ongoing. Starting from non-realistic, freeform structures in the previous section, we have managed to modify the geometry specifications to obtain a manufacturable design, while the optimization algorithm is not endowed with tangible physical features. The steadiness of the response of this design on the -1 st diffraction order, as well as its limited dependence to polarization are additional qualities to its global performance, making it a serious candidate in the landscape of future diffraction devices.

7 Conclusion

In this work, we have extended our topology optimization framework to the full 3D modeling of blazed metasurfaces, enabling the rigorous treatment of nanostructured broadband gratings in reflection. The scattered-field formulation of Maxwell’s equations, discretized with the Finite Element Method and combined with an adjoint-based sensitivity analysis, allows for the efficient optimization of a large number of degrees of freedom within a fixed design region.

A first implementation, referred to as mesh-based, directly associates the density variable to the 3D Finite Element mesh of the design region. This approach fully exploits the versatility of topology optimization and leads to freeform patterns exhibiting outstanding broadband performances, with an average diffraction efficiency of 62% on order -1 over the [400–1,500] nm range for the considered incidence. It highlights the potential of metasurfaces to outperform conventional sawtooth blazed gratings over two octaves. Nevertheless, the resulting geometries in 3D are computationally tremendously heavy, show no significant improvement than conical simulations from our previous work and remain hardly compatible with realistic nanofabrication processes.

To address this limitation, we introduced a second strategy, denoted pillar-based, in which the material distribution is constrained to elementary dielectric pillars compatible with electron-beam lithography and Reactive Ion Etching. The comparison between mesh-based and pillar-based optimizations underlines a central result of this study: while unconstrained 3D topology optimization reveals the ultimate performance limits of broadband blazed metasurfaces, embedding fabrication constraints at the design stage enables a realistic and technologically viable trade-off between efficiency and manufacturability. The obtained metasurface preserves the blazing behavior over a broad spectral range while remaining fully manufacturable. An average efficiency of 57% over two octaves is achieved in s -polarization, with a moderate polarization dependence and a homogeneous spectral

response. This 3D framework therefore establishes a coherent pathway from numerical freeform design to fabricable nanostructured metasurfaces for next-generation spectrographs.

In conclusion, this paper combines Finite Element modeling, topology optimization, and nanofabrication, bridging the gap between theoretical design and real-world manufacturing techniques. Leveraging the concept and tools developed in this work, we can envision new optical functions with specific metasurface designs. Beyond the application to spectroscopy, this framework stands as a versatile tool for the design of advanced metasurfaces. This work is part of the improvements that can be brought in numerous domains of physics and biology, as soon as material characterization is needed. Even though our motivation originates from the need to increase the throughput of spectrographs for astronomy applications, it appears that a tremendous number of fields could utilize our results and tools in the future.

Acknowledgements

This work has been partially supported by CNES and Thales Alenia Space with a PhD grant.

The authors would like to thank Roland Salut, Nicolas Passilly, Andrei Mursa and Quentin Tanguy at FEMTO-ST, Besançon (France) for their work on the fabrication of metasurfaces and their expert advices on our proposed grating. The authors would also like to thank Julien Lumeau and Antonin Moreau at Institut Fresnel, Marseille (France) for the deposition of the layers enabling the fabrication of our grating.

References

- [1] M. W. Farn. Binary gratings with increased efficiency. *Applied Optics*, **31**(22):4453–4458, 1992.
- [2] P. Lalanne, S. Astilean, P. Chavel, et al. Design and fabrication of blazed binary diffractive elements with sampling periods smaller than the structural cutoff. *Journal of the Optical Society of America A*, **16**(5):1143–1156, 1999.
- [3] M. G. Moharam, E. B. Grann, D. A. Pommet, and T. K. Gaylord. Formulation for stable and efficient implementation of the rigorous coupled-wave analysis of binary gratings. *Journal of the Optical Society of America A*, **12**(5):1068–1076, 1995.
- [4] G. Demésy, F. Zolla, A. Nicolet, and B. Vial. Chapter 5: Finite element method. In E. Popov, editor, *Gratings: Theory and Numeric Applications*. Presses Universitaires de Provence, 2nd revisited edition, 2014.
- [5] R. T. Haftka and J. Sobieszczanski-Sobieski. Structural optimization: History. In C. Floudas and P. Pardalos, editors, *Encyclopedia of Optimization*. Springer, Boston, 2004.
- [6] G. Allaire, E. Bonnetier, G. Francfort, and F. Jouve. Shape optimization by the homogenization method. *Numerische Mathematik*, **76**:27–68, 1997.
- [7] G. Allaire, C. Dapogny, and P. Frey. Shape optimization with a level set based mesh evolution method. *Computer Methods in Applied Mechanics and Engineering*, **282**:22–53, 2014.
- [8] E. Kuci, F. Henrotte, P. Duysinx, and C. Geuzaine. Design sensitivity analysis for shape optimization based on the Lie derivative. *Computer Methods in Applied Mechanics and Engineering*, **317**:702–722, 2017.
- [9] M. P. Bendsøe and N. Kikuchi. Generating optimal topologies in structural design using a homogenization method. *Computer Methods in Applied Mechanics and Engineering*, **71**:197–224, 1988.
- [10] M. P. Bendsøe and O. Sigmund. Topology optimization by distribution of isotropic material. In *Topology Optimization: Theory, Methods, and Applications*. Springer Berlin Heidelberg, 2008.
- [11] T. Borrvall and J. Petersson. Topology optimization of fluids in Stokes flow. *International Journal for Numerical Methods in Fluids*, **41**:77–107, 2003.
- [12] I. Castañar, J. Baiges, and R. Codina. Topology optimization of incompressible structures subject to fluid-structure interaction. *Structural and Multidisciplinary Optimization*, **67**:90, 2024.
- [13] J. S. Jensen. A simple method for coupled acoustic-mechanical analysis with application to gradient-based topology optimization. *Structural and Multidisciplinary Optimization*, **59**(5):1567–1580, 2019.
- [14] V. Cool, O. Sigmund, N. Aage, et al. Vibroacoustic topology optimization for sound transmission minimization through sandwich structures. *Journal of Sound and Vibration*, **568**:117959, 2024.

- [15] E. Kuci, F. Henrotte, P. Duysinx, and C. Geuzaine. Combination of topology optimization and Lie derivative-based shape optimization for electro-mechanical design. *Structural and Multidisciplinary Optimization*, **59**(5):1723–1731, 2019.
- [16] X. Qian and O. Sigmund. Topological design of electromechanical actuators with robustness toward over- and under-etching. *Computer Methods in Applied Mechanics and Engineering*, **253**(10):237–251, 2013.
- [17] K. Friis and O. Sigmund. Robust topology design of periodic grating surfaces. *Journal of the Optical Society of America B*, **29**(10):2935–2943, 2012.
- [18] Y. Deng and J. G. Korvink. Self-consistent adjoint analysis for topology optimization of electromagnetic waves. *Journal of Computational Physics*, **361**:353–376, 2018.
- [19] J. L. Pita Ruiz, A. S. A. Amad, L. H. Gabrielli, and A. A. Novotny. Optimization of the electromagnetic scattering problem based on the topological derivative method. *Optics Express*, **27**(23):33586–33605, 2019.
- [20] M. P. Bendsøe and O. Sigmund. Material interpolation schemes in topology optimization. *Archive of Applied Mechanics*, **69**(10):635–654, 1999.
- [21] J. Jiang, E. Lupoiu, E. W. Wang, et al. MetaNet: a new paradigm for data sharing in photonics research. *Optics Express*, **28**(9):13670–13681, 2020.
- [22] Z. Li, R. Pestourie, Z. Lin, et al. Empowering metasurfaces with inverse design: principles and applications. *ACS Photonics*, **9**(7):2178–2192, 2022.
- [23] R. Marzban, H. Abiri, R. Pestourie, and A. Adibi. HiLAB: A Hybrid Inverse-Design Framework. *Small Methods*, **9**(11):e00975, 2025.
- [24] D. Sell, J. Yang, S. Doshay, and J. A. Fan. Periodic Dielectric Metasurfaces with High-Efficiency, Multiwavelength Functionalities. *Advanced Optical Materials*, **5**:1700645, 2017.
- [25] F. Burmeister, T. Flügel-Paul, U. D. Zeitner, et al. Binary blazed reflection grating for UV/VIS/NIR/SWIR spectral range. In *Proceedings of SPIE 11180, International Conference on Space Optics – ICSSO 2018*, page 111801J, 2018.
- [26] Y. Xiao, M. Xu, M. Pu, et al. Topology-optimized freeform broadband optical metagrating for high-efficiency large-angle deflection. *Journal of the Optical Society of America B*, **41**(2):A52–A59, 2024.
- [27] S. Ans, F. Zamkotsian, and G. Demésy. Topology optimization of blazed gratings under conical incidence. *Journal of the Optical Society of America A*, **41**(8):1531–1543, 2024.
- [28] C. Geuzaine and J. F. Remacle. Gmsh: a three-dimensional finite element mesh generator with built-in pre- and post-processing facilities. *International Journal for Numerical Methods in Engineering*, **79**(11):1309–1331, 2009.
- [29] P. Dular, C. Geuzaine, F. Henrotte, and W. Legros. A general environment for the treatment of discrete problems and its application to the finite element method. *IEEE Transactions on Magnetics*, **34**(5):3395–3398, 1998.
- [30] S. Ans, G. Demésy, F. Zamkotsian, et al. Nanostructured blazed gratings for high performance spectrographs. In *Proceedings of SPIE 12990, SPIE Photonics Europe – Metamaterials XIV*, page 129900K, 2024.
- [31] S. Ans, G. Demésy, F. Zamkotsian, et al. Nanostructured blazed gratings for high-efficiency spectrographs by topology optimization. In *Proceedings of SPIE 13669, ICSSO – International Conference on Space Optics*, page 136693B, 2025.
- [32] R.E. Christiansen, J. Vester-Petersen, S. P. Madsen, and O. Sigmund. A non-linear material interpolation for design of metallic nano-particles using topology optimization. *Computer Methods in Applied Mechanics and Engineering*, **343**:23–29, 2021.
- [33] F. Zolla. Section 3.4: Ondes propagatives. In *Contribution à l'étude de la diffraction et de l'adsorption des ondes électromagnétiques : Structures bipériodiques minces, structures cylindriques par la méthode des sources fictives*. PhD thesis, Aix-Marseille Université, 1993.
- [34] J. Gedeon, E. Hassan, and A. C. Lesina. Time-domain topology optimization of arbitrary dispersive materials for broadband 3D nanophotonics inverse design. *ACS Photonics*, **10**:3875–3887, 2023.
- [35] B. Vial and Y. Hao. Open-source computational photonics with auto-differentiable topology optimization. *Mathematics*, **10**(20):3912, 2022.
- [36] M. Huff. Recent advances in Reactive Ion Etching and applications of high-aspect-ratio microfabrication. *Micro-machines*, **12**:991, 2021.

Appendix

The 3D mesh-based optimized pattern achieved with our solver shows outstanding performance for blazed gratings. However we have observed that running the optimization with the same parameters (angles of incidence, targeted wavelengths, material, etc.) with our conical solver yields a very close optimized pattern, regarding its shape and response. The latter is plotted in the paper (see Fig. 5) but for the sake of clarity, we did not display the pattern itself. We only mentioned that it is close to the conical one. This appendix provides additional results to this part.

Figure 9a shows a side view of the 3D pattern to illustrate that the obtained shape closely corresponds to that of the output of the same optimization with a conical solver, meaning the mono-periodic grating shown in Fig. 9b. The degree of freedom along the x axis is harnessed though, with a variation of shape between $x_{\min} = 0$ and $x_{\max} = 330$ nm.

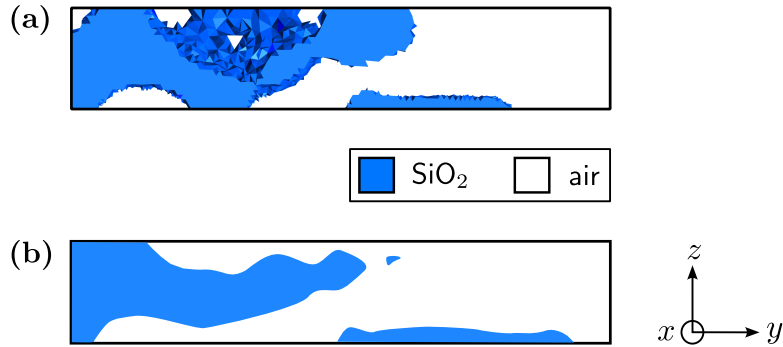


Figure 9: (a) Side view of the 3D optimized pattern with the set of 17 targeted wavelengths displayed in the paper (Fig. 5). (b) Achieved pattern with the exact same optimization, but with a conical solver. The boundaries have been smoothed, for the mesh is twice finer than in 3D.

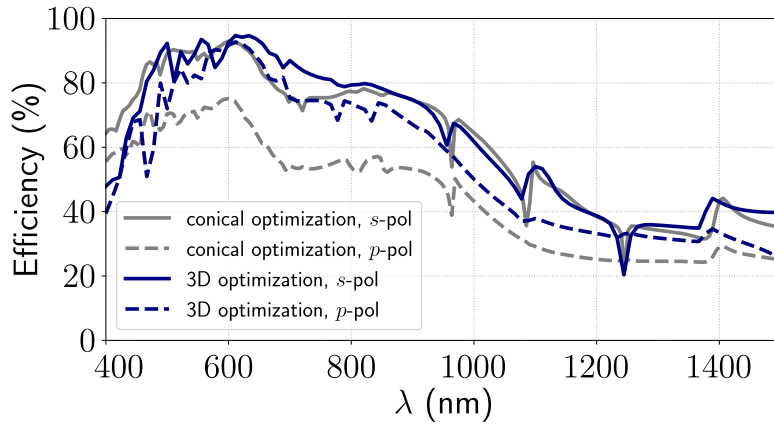


Figure 10: Spectral response of the bi-periodic grating of Fig. 9a (blue lines) and the mono-periodic grating of Fig. 9b (gray lines), for s -polarization $\psi_i = 0^\circ$ (solid lines) and p -polarization $\psi_i = 90^\circ$ (dashed lines).

Unfortunately, this variation of shape does not improve the overall blazing effect, as shown by the plot of Fig. 5c (blue vs. gray curve). However, the polarization dependence is much lower with the 3D pattern, as illustrated in Fig. 10. In this graph, the p -polarization $\psi_i = 90^\circ$ (dashed lines) is added to the s -polarization from Fig. 5c of the article (solid lines).

In conclusion, the bi-periodic pattern is more satisfactory, for it is mechanically sustainable and shows low polarization dependence, but it takes 10 days to run this optimization (vs. 9 hours for a conical study), yielding a result that still shows challenging shapes for manufacturing.